Natural marine bromoform emissions in the fully coupled ocean-atmosphere-model NorESM2

Dennis Booge[1,2], Jerry F. Tjiputra[3], Dirk J. L. Olivié[4], Birgit Quack[1] and Kirstin Krüger[2]

[1]GEOMAR Helmholtz Centre for Ocean Research Kiel, Kiel, 24148, Germany
[2]Department of Geosciences, Section of Meteorology and Oceanography, University of Oslo, Oslo, 0371, Norway
[3]NORCE Norwegian Research Centre and Bjerknes Centre for Climate Research, Bergen, 5007, Norway
[4]Norwegian Meteorological Institute, Oslo, 0313, Norway

Correspondence to: Dennis Booge (dbooge@geomar.de) and Kirstin Krüger (kkrueger@geo.uio.no)

Abstract. Oceanic bromoform ($CHBr_3$) is an important precursor of atmospheric bromine. Although highly relevant for the future halogen burden and ozone layer in the stratosphere, the global $CHBr_3$ production in the ocean and its emissions are still poorly constrained in observations and are mostly neglected in climate models. Here, we newly implement marine $CHBr_3$ in the state-of-the-art Norwegian Earth System Model (NorESM2) with fully coupled ocean-sea-ice-atmosphere biogeochemistry interactions. Our results are validated with oceanic and atmospheric observations from the HalOcAt (Halocarbons in the Ocean and Atmosphere) data base. The simulated mean oceanic concentrations (6.61 ± 3.43 pmol L^{-1}) are in good agreement with observations in open ocean regions (5.02 ± 4.50 pmol L^{-1}), while the mean atmospheric mixing ratios (0.76 ± 0.39 ppt) are lower than observed but within the range of uncertainty (1.45 ± 1.11 ppt). The NorESM2 ocean emissions of $CHBr_3$ (214 Gg yr^{-1}) are in the range of or higher than previously published estimates from bottom-up approaches but lower than estimates from top-down approaches. Annual mean fluxes are mostly positive (sea-to-air), driven by oceanic concentrations, sea surface temperature and wind speed, dependent on season and location. During winter , model results imply some oceanic regions in high latitudes as sinks of atmospheric $CHBr_3$, because of its elevated atmospheric mixing ratios. We further demonstrate that key drivers for the oceanic and atmospheric $CHBr_3$ variability are spatially heterogeneous. In the tropical West Pacific, which is a hot spot for oceanic bromine delivery to the stratosphere, wind speed is the main driver for $CHBr_3$ fluxes on annual basis. In the North Atlantic as well as in the Southern Ocean region the atmospheric and oceanic $CHBr_3$ variabilities are interacting during most of the seasons except for the winter months where sea surface temperature is the main driver. Our study provides improved process understanding of the biogeochemical cycling of $CHBr_3$ and more reliable natural emission estimates especially on seasonal and spatial scales compared to previously published model estimates.

1   Introduction

Bromoform ($CHBr_3$) from the ocean is one of the most important organic compounds for atmospheric bromine with an atmospheric lifetime of ~2-4 weeks (Carpenter and Liss, 2000; Quack and Wallace, 2003; Salawitch, 2006; Papanastasiou et al., 2014). As a reactive halogenated compound, it belongs to the very short-lived substances (VSLS) with lifetimes of less than 6 months in the atmosphere (Law et al., 2007). In the tropics, VSLSs are rapidly lifted to the stratosphere by deep convection (Sala et al., 2014; Navarro et al., 2015; Fuhlbrügge et al., 2016), where they contribute up to ~25% to stratospheric bromine (Dorf et al., 2006 and following work). Bromine is ~60 times more efficient in depleting lower stratospheric ozone than chlorine and significantly contributes to ozone depletion in the lower stratosphere (Daniel et al., 1999; Sinnhuber et al., 2009; Montzka et al., 2011; Villamayor et al., 2023) with potential impacts on the radiation budget of the atmosphere from -0.02 W m^{-2} to -0.13 W m^{-2} (Hossaini et al., 2015; Saiz-Lopez et al., 2023).

The oceanic air-sea gas exchange of $CHBr_3$ is parameterized based on the concentration gradient between surface water and air and is related to wind speed and sea surface temperature via the transfer velocity (e.g., Nightingale et al., 2000).

41 Due to sparse measurements, marine $CHBr_3$ emission estimates are subject to large uncertainties (Laube et al., 2023).

42 $CHBr_3$ emission inventories from "bottom-up" approaches (e.g., Quack and Wallace, 2003; Butler et al., 2007; Ziska et

43 al., 2013; Lennartz et al., 2015; Stemmler et al., 2015; Fiehn et al., 2018) are based on in-situ oceanic data, whereas "top-

44 down" approaches (e.g., Warwick et al., 2006; Liang et al., 2010; Ordóñez et al., 2012) use in situ atmospheric mixing

45 ratio measurements. Resulting $CHBr_3$ emissions span a large range between 150 and 820 Gg Br yr^{-1} (Laube et al., 2023).

46 The different methods cover e.g., statistical extrapolation of measurement-based data (Ziska et al., 2013; and update in

47 Fiehn et al., 2018), scaling of emissions to chlorophyll-a satellite observations (Ordóñez et al., 2012), modelling

48 atmospheric $CHBr_3$ with a modular flux in a chemistry climate model (Lennartz et al., 2015), and a data-oriented machine-

49 learning algorithm (Wang et al., 2019). These studies use limited spatial and temporal data coverage, underrepresenting

50 seasonal and interannual variations and spatial heterogeneity by averaging concentrations.

51 Oceanic $CHBr_3$ is mainly linked to primary production through natural processes such as marine organisms like

52 macroalgae and phytoplankton (Gschwend et al., 1985; Carpenter and Liss, 2000; Quack et al., 2004). Elevated surface

53 water concentrations are observed in coastal and shelf waters especially including the eastern boundary upwelling systems

54 (EBUS) (Quack and Wallace, 2003). Laboratory culture studies of phytoplankton production rates by Tokarczyk and

55 Moore (1994) and Moore et al. (1996) reported $CHBr_3$ increase during the exponential growth phase of phytoplankton.

56 Those specific growth rates and the corresponding temporal changes in $CHBr_3$ concentrations were first applied in a

57 physical biogeochemical water column model for the tropical Atlantic (Hense and Quack, 2009), and later implemented

58 in the global biogeochemical HAMburg Ocean Carbon Cycle model (HAMOCC; Stemmler et al., 2015). Stemmler et al.

59 (2015) explicitly implemented sources and sinks of marine $CHBr_3$ in the three-dimensional ocean biogeochemistry model

60 HAMOCC. However, they are not fully coupled with the atmosphere, and resulting fluxes rely on fixed, prescribed,

61 extrapolated, observed atmospheric data of Ziska et al. (2013). Since the atmospheric concentrations are regulated by the

62 oceanic emissions, accurate estimates of atmospheric and oceanic $CHBr_3$ variability require such coupling, which can be

63 achieved using an Earth System Model (ESM).

64 Here, we present the first global model simulation of $CHBr_3$ in the fully coupled Norwegian ESM (NorESM2), where

65 $CHBr_3$ production is prognostically related to the primary production in the ocean taking natural biological processes into

66 account. We present results from a historical experiment focusing on the period 1990 to 2014 and compare them with

67 HalOcAt observations (https://halocat.geomar.de). Furthermore, we evaluate oceanic $CHBr_3$ excess and deficit regions

68 and use multilinear regression analysis to identify drivers of oceanic and atmospheric $CHBr_3$, as well as $CHBr_3$ emission

69 variations on regional and temporal scales.

70 **2 Model and Methods**

71 We use the latest version of NorESM2 (NorESM2-LM; Seland et al., 2020; Tjiputra et al., 2020), which has participated

72 in the Coupled Model Intercomparison Project phase 6 (CMIP6) and contributed to the latest assessment report of the

73 IPCC-AR6 (Masson-Delmotte et al., 2023). The NorESM2 is a fully coupled ESM and is partly based on the Community

74 ESM Version 2 (Danabasoglu et al., 2020), which is developed by the National Center for Atmospheric Research (NCAR)

75 in the United States. NorESM2 is an updated version of its original version NorESM1 (Bentsen et al., 2013; Tjiputra et

76 al., 2013). It consists of a modified version of the Community Atmosphere Model version 6 (CAM6-Nor), the isopycnic

77 coordinate Bergen Layered Ocean Model (BLOM), the ocean biogeochemistry model isopycnic coordinate HAMOCC

78 (iHAMOCC), the sea ice model (Community Ice CodE version 5.1.2; CICE5.1.2), the Community Land Model version

79 5 (CLM5), and the river runoff model (MOdel for Scale Adaptive River Transport; MOSART). Both BLOM and

80 iHAMOCC apply a tripolar grid with a horizontal resolution of ~1° and 53 vertical isopycnic layers, while CAM6-Nor

81 and CLM5 share a common horizontal resolution of ~2° and 32 hybrid-pressure layers (lowest atmospheric layer

thickness: ~120 m) and a model top at 3.6 hPa (~40 km altitude). Here, we briefly highlight key features of iHAMOCC as well as the CHBr$_3$ implementation (Section 2.1). The iHAMOCC ocean biogeochemical module is based on the original work of Maier-Reimer (2012), has gone through several improvements and was later adapted to an isopycnic coordinate ocean model (Assmann et al., 2010; Tjiputra et al., 2010). The model prognostically simulates inorganic carbon chemistry following the standard Ocean Model Intercomparison Project (OMIP) protocol. It includes a Nutrient Phytoplankton Zooplankton Detritus (NPZD) type ecosystem module, where the phytoplankton growth rate is constrained by multi-nutrient limitation as well as ambient light and temperature. Particulate organic matters produced in the euphotic zone is exported to the interior with a sinking velocity that increases linearly with depth before it is remineralized back to inorganic carbon. The NorESM2 is able to simulate the observed large-scale pattern of surface primary productivity as well as the regional seasonal cycle (Tjiputra et al., 2020).

2.1 Bromoform module in NorESM2

2.1.1 Oceanic bromoform

The marine CHBr$_3$ processes implemented in iHAMOCC comprise of advection and other physical processes (*adv*), production (*β*), air-sea gas exchange (*F*), and three sink terms of: photolysis (*UV*), hydrolysis (*H*) and halogen substitution (*S*), as shown in Eq. (1). The production and photolysis occur in the euphotic layer (top 100 m depth) of the model, whereas the air-sea gas exchange is computed in the top-most layer of the ocean (upper 10 m). Advection and other sink terms are calculated throughout the water column. The change over time of the oceanic CHBr$_3$ concentration is modelled as:

$$\frac{d[\text{CHBr}_3]}{dt} = adv + \beta - F - UV - H - S. \tag{1}$$

The parameterizations for the different processes are largely based on Stemmler et al. (2015). CHBr$_3$ is produced during biological production as follows:

$$\beta = \beta_0 * (\frac{f_1 * Si(OH)_4}{K_{phy}^{Si(OH)_4} + Si(OH)_4} + \frac{f_2 * K_{phy}^{Si(OH)_4}}{K_{phy}^{Si(OH)_4} + Si(OH)_4}), \tag{2}$$

where $K_{phy}^{Si(OH)_4}$ denotes the half-saturation constant for silicate (Si(OH)$_4$) uptake and diatom and non-diatom contributing factors, f_1 and f_2, are set equally to 1. In contrast to Stemmler et al. (2015), the bulk CHBr$_3$ production ratio (β_0) is modified and set to 2.4x10^{-6} nmol CHBr$_3$ (mmol N)$^{-1}$, based on Kurihara et al. (2012) and Roy (2010).

The air-sea gas exchange is calculated as follows:

$$F = k_w * (C_w - \frac{C_a}{H_{bromo}}), \tag{3}$$

where C_w and C_a are CHBr$_3$ concentrations in the surface ocean and CHBr$_3$ mixing ratios in the atmosphere, respectively. Emissions are defined as positive fluxes, which means outgassing to the atmosphere, negative fluxes are defined as fluxes from the atmosphere to the ocean . The temperature-dependent dimensionless Henry's law solubility constant (H_{bromo}) is defined in Moore et al. (1995):

$$H_{bromo} = e^{13.16 - \frac{4973}{SST}}, \tag{4}$$

with SST the sea-surface temperature in Kelvin. k_w represents the gas transfer velocity calculated following Nightingale et al. (2000) using the 10 m surface wind speed (*u*):

$$k_w = (0.222u^2 + 0.33u) * (\frac{660}{Sc_{bromo}})^{0.5}. \tag{5}$$

116

117 The Schmidt number (Sc_{bromo}) for $CHBr_3$ is defined in Quack and Wallace (2003) using the sea surface temperature *SST*

118 in °C:

$$Sc_{bromo} = 4662.8 - 319.45 * SST + 9.9012 * SST^2 - 0.1159 * SST^3. \tag{6}$$

119

120 The loss term due to photolysis is computed as follows:

$$UV = I_{UV} * \frac{I_0}{I_{ref}} * e^{(-a_w * z)} * [CHBr_3], \tag{7}$$

121

122 where the decay time scale $(I_{UV})^{-1}$ is set to 30 days (Carpenter and Liss, 2000). I_0 and I_{ref} are the prognostic incoming UV

123 radiation (i.e., 30% of shortwave radiation) and annual average irradiance at the surface layer, respectively. *z* is the depth

124 and a_w is the attenuation coefficient of UV radiation, set to 0.33 m^{-1}.

125 The loss term related to hydrolysis is estimated following Stemmler et al. (2015):

$$H = A_1 * e^{\left(-\frac{E_A}{RT}\right)} * [OH^-] * [CHBr_3], \tag{8}$$

126

127 with A_1, E_A, and *R* set to 1.23x10^{17} L mol^{-1} min^{-1}, 107 300 J mol^{-1}, and 8.314 J K^{-1} mol^{-1}, respectively (Washington, 1995).

128 *T* is the seawater temperature in Kelvin.

129

130 Degradation due to halogen substitution (Eqs. 5-6 of Stemmler et al., 2015):

$$S = L_{ref} * e^{\left(A_2 * (\frac{1}{T_{ref}} - \frac{1}{T})\right)} * [CHBr_3], \tag{9}$$

131

132 with L_{ref} and A_2 set to 7.33x10^{-10} s^{-1} and 12507.13 K, respectively, and T_{ref} = 298 K.

133 ### 2.1.2 Atmospheric CHBr$_3$

134 CHBr$_3$ is implemented as a 3-dimensional tracer in the atmospheric model and is transported by the large-scale

135 atmospheric circulation and sub-grid scale processes (shallow and deep convection, and boundary layer turbulence). It is

136 removed in the atmosphere by photolysis:

$$CHBr_3 + hv \rightarrow 3\,Br, \tag{10}$$

137

138 and by reaction with the OH radical:

$$CHBr_3 + OH \rightarrow 3\,Br. \tag{11}$$

139

140 The reaction rate *k* [cm^3 molecules^{-1} s^{-1}] for the removal of CHBr$_3$ by OH in

$$\frac{d[CHBr_3]}{dt} = -k * [CHBr_3] * [OH] \tag{12}$$

141

142 is defined as follows:

$$k = 9.0 * 10^{-13} \exp\left(-\frac{360}{T}\right),$$ (13)

with T the ambient temperature in Kelvin, and $[CHBr_3]$ and $[OH]$ in molecules cm^{-3}. The loss rate of $CHBr_3$ by photolysis can be expressed by

$$\frac{d[CHBr_3]}{dt} = -I \, [CHBr_3],$$ (14)

where I [s^{-1}] depends on the intensity of solar radiation and photo-physical properties of $CHBr_3$. The OH concentration is a monthly-varying climatology obtained from a Whole Atmosphere Community Climate Model (WACCM) historical simulation with full tropospheric and stratospheric chemistry (Gettelman et al., 2019).

$CHBr_3$ in the atmosphere has no other sinks than reaction with OH (annual mean $CHBr_3$ lifetime: ~46 days) and photolysis ($CHBr_3$ lifetime: ~23 days) and is not affected by dry or wet deposition.

2.2 Model setup

A historical transient model run from 1850-2014, based on the CMIP6 protocol, was performed following a 500-year preindustrial spin-up. The coupling of $CHBr_3$ between the ocean and the atmosphere is carried out with an hourly time frequency exchanging the air-sea gas transfer. For analysis of the model climatology as well as for analysis of the model validation with observations and further analysis of the driving $CHBr_3$ factors, daily model output data was averaged over a period of 25 years (1990-2014) resulting in one mean value for each day of the year. The standard deviation of each day reflects the variability within this time period. The 1990 to 2014 interval was chosen as most of the observations for the model validation are within that time period, as compiled in the HalOcAt database (https://halocat.geomar.de, last access: 13.10.2023).

2.3 Observations: HalOcAt database

The HalOcAt database, compiled by Ziska et al. (2013), updated by Fiehn et al. (2018) and by this study, is an observation-based database for global oceanic and atmospheric data of short-lived halogenated compounds, such as $CHBr_3$. To date, there are 9369 oceanic and 65179 atmospheric $CHBr_3$ measurements listed in 68 oceanic and 156 atmospheric datasets (campaigns), respectively. The following criteria were applied to the observations in order to be used for model validation:

- Sampling locations with an ocean bottom depth less than 200 m or closer than 100 km to land were excluded.
- Sampling depth of oceanic $CHBr_3$ measurements had to be within the first 10 m of the water column in order to be comparable to the $CHBr_3$ output of the upper surface ocean model layer (10 m depth).
- Maximum sampling height of atmospheric $CHBr_3$ measurements was set to 30 m altitude.
- Wherever applicable, individual measurements throughout one day were averaged to result in a daily averaged surface ocean concentration or atmospheric mixing ratio in order to consider the same temporal resolution as the daily model output. The coordinates of the respective averaged data points throughout a day were also equally averaged. These locations were used to compare the observation with the closest grid point of the model output.

174
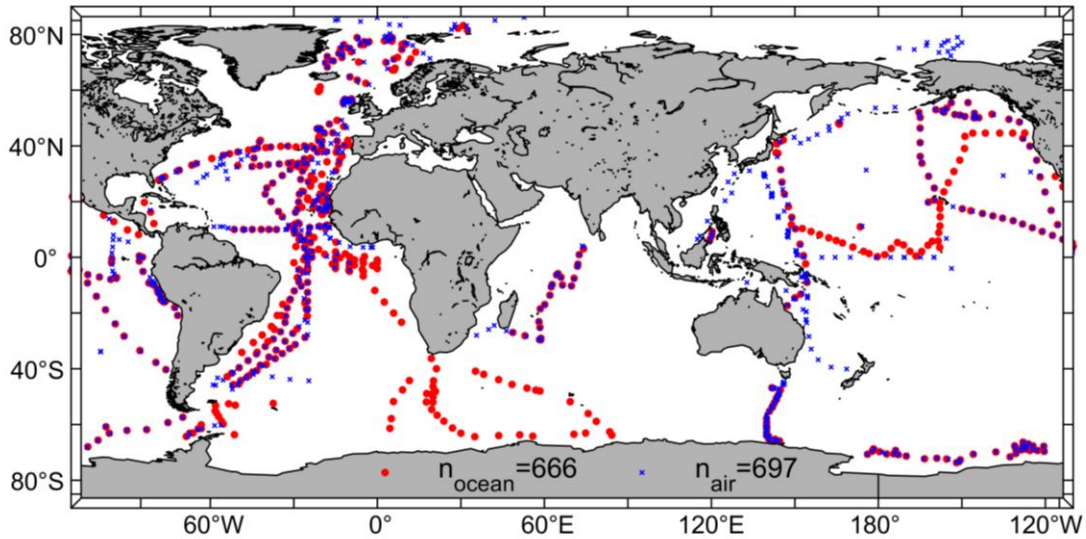
Figure 1: Locations of oceanic (red, n=666) and atmospheric (blue, n=697) daily mean CHBr₃ observations from the HalOcAt database used to compare to daily mean NorESM2 model output.

175 After screening the HalOcAt data base with the above-mentioned criteria, the individual oceanic and atmospheric datasets

176 (including the remaining datapoints) were tested for outliers. The mean from each dataset was calculated and the group

177 of all average values was tested for outliers. An outlier was defined as an element with more than three standard deviations

178 from the mean. According to the outlier test for oceanic and atmospheric datasets the corresponding dataset was removed

179 and not used for further validation of the model.

180 By addressing the mentioned criteria and datasets, we were able to validate the model with 666 daily mean oceanic (5154

181 individual) and 697 daily mean atmospheric (8411 individual) CHBr₃ observations from the HalOcAt database covering

182 both hemispheres (northern hemisphere (NH): 61%, southern hemisphere (SH): 39%), from the tropics (0-20°N/°S; 36%)

183 to the polar regions (60-90°N/S; 18%) with most observations in or above the Atlantic Ocean (44%) (Figure 1).

184 **2.4 Bromoform excess/deficit calculation**

185 The CHBr₃ excess/deficit (balance) rate (k_{bal}, Eq. (15), pmol m^{-2} h^{-1}) is the difference between the CHBr₃ production rate

186 and the sum of different CHBr₃ loss rates, with all rates integrated over the upper 100 m depth):

$$k_{bal} = \sum production\ rate - \sum loss\ rate = k_\beta - (k_{UV} + k_F). \tag{15}$$

187

188 The production term is described as the biological oceanic CHBr₃ production rate (k_β, Eq. (2)) and the loss term includes

189 the two fastest loss processes, i.e., photolysis due to UV radiation (k_{UV}, Eq. (7)) and the loss to the atmosphere via air-sea

190 gas exchange (k_F, Eq. (3)). We define a positive k_{bal} as CHBr₃ excess rate and a negative k_{bal} as CHBr₃ deficit rate. The

191 loss terms related to hydrolysis and to halogen substitution are not included as they are several orders of magnitude

192 smaller than k_{UV} and k_F, in the surface ocean.

193 **2.5 Calculation of drivers for oceanic and atmospheric CHBr₃ and its emissions**

194 Different parameters impact the variations of oceanic and atmospheric CHBr₃ values and influence the air-sea gas

195 exchange. These impacts can vary in magnitude and frequency dependent on local and seasonal conditions. Daily mean

196 average model output values from 1990-2014 were used to calculate annual and seasonally resolved (DJF, MAM, JJA,

197 SON) driving factors for oceanic CHBr₃ concentrations (*Bromo_oce*), atmospheric CHBr₃ mixing ratios (*Bromo_air*) and

198 CHBr₃ fluxes (*Bromo_flux*) in three different specific areas (North Atlantic, tropical West Pacific, Southern Ocean), which

199 are presented in Section 3.4. Driving factors for each area, parameter and season were derived using multilinear regression

200 (MLR) analyses.

201 In order to compare parameters with different magnitudes, input data of each parameter was standardized prior to MLR

202 analysis by centering to have a mean of 0 and scaled to have a standard deviation of 1. Input data for each parameter

203 consisted of daily mean averages over the specific area, providing 365 values as basis for annually and ~ 90 values for

204 seasonally resolved MLR.

205 A schematic summarizing the relationships between the different parameters in Eqs. (S1-S3) is shown in Fig. 2 including

206 CHBr$_3$ production ($Bromo_{prod}$), the 10 m surface wind speed ($wind$), the sea surface temperature (SST) and the derived
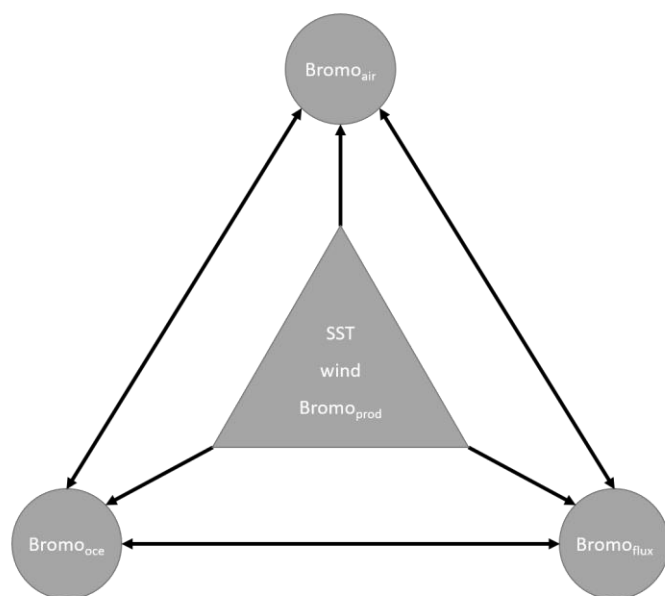
Figure 2: Schematic illustration of relationships between different parameters influencing each other. Generic parameters in triangle influence the derived parameters in circles. Each derived parameter in a circle is influenced by all other five parameters. Relationships are the basis for the multilinear regression analysis using Eqs. (S1-S3).

207 parameters $Bromo_{oce}$, $Bromo_{air}$ and

208 $Bromo_{flux}$. Other oceanic CHBr$_3$ loss

209 processes (e.g., photolysis) were neglected

210 in these calculations as the loss due to gas

211 exchange is ~70 times higher than the loss

212 due to photolysis (data not shown). If the

213 highest resulting coefficient for each season

214 and MLR is significantly higher than all

215 other coefficients, the corresponding

216 parameter is presented as the main driver for

217 either $Bromo_{oce}$, $Bromo_{air}$ or $Bromo_{flux}$. If the

218 highest resulting coefficient is not

219 significantly different from the second or

220 third highest coefficient, more than one

coefficient and corresponding parameters

are presented as main drivers. Table 1 lists

the annual mean coefficients, Table S1 lists

224 the seasonally resolved main drivers.

225

3 Results and Discussion

3.1 Model climatology

228 The annual and seasonal CHBr$_3$ oceanic concentrations, atmospheric mixing ratios and emissions reveal significant

229 spatial variations (Figure 3, S1). The annual global average surface CHBr$_3$ concentrations are 5.04 pmol L^{-1} (DJF:

230 5.36 pmol L^{-1}, JJA: 4.86 pmol L^{-1}) with highest annual mean concentrations of 28.37 pmol L^{-1} in the upwelling region off

231 the coast of Peru and lowest annual mean concentrations of 1.37 pmol L^{-1} in the Gulf of Boothia (71°N, 91°W) north of

232 Canada. The areas with the lowest oceanic CHBr$_3$ concentrations are the central parts of the North and the South Pacific

233 Gyres. Concentrations of surface ocean CHBr$_3$ in the entire NH (JJA: 5.9 pmol L^{-1} > DJF: 4.3 pmol L^{-1}) and SH (DJF:

234 6.1 pmol L^{-1} > JJA: 4.1 pmol L^{-1}) are generally higher during the respective summer than during the respective winter.

235 These distinct differences of oceanic CHBr$_3$ concentrations are also due to the higher biological production in summer

236 (NH: 335 pmol m^{-2} h^{-1}; SH: 371 pmol m^{-2} h^{-1}) than in winter (NH: 235 pmol m^{-2} h^{-1}; SH: 173 pmol m^{-2} h^{-1}) as shown in

237 Fig. S3 and discussed in Section 3.4. The direct link of CHBr$_3$ to the biological production applies to the low oceanic

238 CHBr$_3$ concentrations in the North and South Pacific Gyres and to the high oceanic concentrations in the areas of the

239 EBUS.

240 Variations in annual mean atmospheric $CHBr_3$ mixing ratios mainly follow the surface ocean concentrations with highest

241 mixing ratios in the tropics, especially in the EBUS. Global annual average mixing ratios over the ocean are 0.67 ppt

242 (DJF: 0.70 ppt, JJA: 0.69 ppt) with highest annual mean mixing ratios of 2.21 ppt in the south-eastern Pacific upwelling

243 region off the coast of Peru and lowest annual mean mixing ratios of 0.13 ppt over the Persian Gulf. On a global average,

244 the variability of atmospheric mixing ratios is lower than the variability of $CHBr_3$ concentrations in the surface ocean

245 (Figure 3, S2). During austral winter (JJA), mostly dark and cold conditions increase the lifetime of atmospheric $CHBr_3$,

246 which leads to a uniform mixing ratio (0.67 ± 0.05 ppt) over the entire Southern Ocean. Similar to oceanic $CHBr_3$

247 concentrations, central parts of the North and South Pacific Gyre have low atmospheric $CHBr_3$ mixing ratios

248 (0.46 ± 0.05 ppt). During austral summer (DJF) atmospheric mixing ratios increase further as strong biological activity

249 increases surface ocean concentrations, which enhance the oceanic emissions. Further seasonal dependent driving factors

250 for specific regions are discussed in Section 3.4.

251 Generally, supersaturation of $CHBr_3$ in the world's ocean leads to emissions from the ocean to the atmosphere (defined

252 as positive fluxes). Global annual mean fluxes are 268 pmol m^{-2} h^{-1} (DJF: 294 pmol m^{-2} h^{-1}, JJA: 253 pmol m^{-2} h^{-1}) with

253 highest annual mean fluxes of 953 pmol m^{-2} h^{-1} in the upwelling region off the coast of Peru. In the tropical regions,

254 annual mean fluxes of 427 pmol m^{-2} h^{-1} between 10°N and 10°S, add to atmospheric entrainment of oceanic $CHBr_3$ up

255 into the stratosphere (Fiehn et al., 2018; Tegtmeier et al., 2020). Lowest annual mean fluxes of -1 pmol m^{-2} h^{-1} are

256 modelled under ice free conditions in the Gulf of Boothia (71°N, 91°W) north of Canada (white regions in Figure 3) with

257 very low oceanic $CHBr_3$ production and low seawater temperatures. However, the atmospheric mixing ratios are

258 comparably high under these conditions. These conditions favour negative fluxes, which, according to the results of our

259 fully coupled ESM, can be seen in the Arctic and Antarctic during winter, confirming the results by Stemmler et al. (2015)

260 and Ziska et al. (2013) although with a lower magnitude.

261 Generally, the modelled $CHBr_3$ emissions are high, where the ocean concentration is high and the elevated emissions lead

262 to elevated atmospheric mixing ratios. However, due to oceanic transport processes, locations of high oceanic $CHBr_3$

263 emissions do not always coincide with locations of high oceanic $CHBr_3$ production (compare Figure 3 and Fig. S3). In

264 the northern part of the Bay of Bengal (>18°N) e.g., ocean concentrations during DJF are very high (average:

265 21.64 pmol L^{-1}), while the emissions are not as high compared to other ocean regions, due to low wind speeds. This leads

266 to a lower atmospheric mixing ratio than expected from the oceanic concentrations and shows that oceanic $CHBr_3$

267 concentrations and emissions as well as atmospheric mixing ratios show regionally different interdependencies, which is

268 addressed in detail in Section 3.4.

269
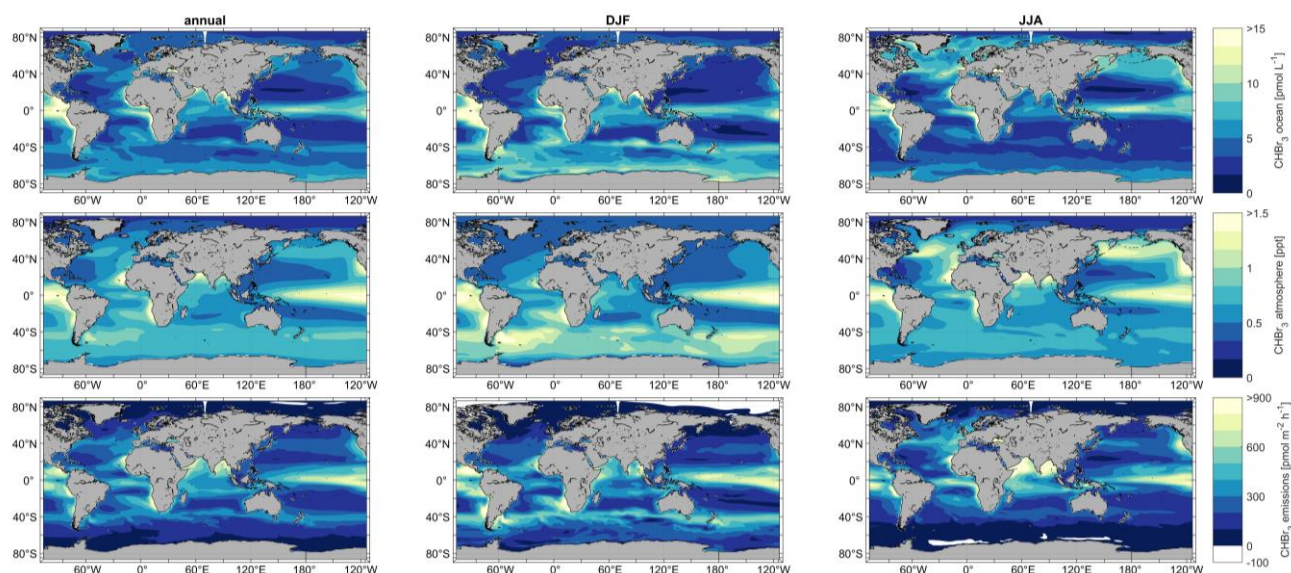
Figure 3: Simulated annual (left), DJF (middle) and JJA (right) mean oceanic surface CHBr₃ concentrations (upper panel), atmospheric mixing ratios (middle panel) and CHBr₃ emissions (lower panel) for the period 1990-2014.

3.2 Model validation with observations

The annual mean surface oceanic CHBr$_3$ concentration (Figure 4a) from the 666 daily mean observations is $5.02^{28.21}_{0.05}$ (mean$^{max}_{min}$) pmol L^{-1}. The global annual mean surface oceanic CHBr$_3$ concentration from the model using only locations corresponding with an existing observation is $6.61^{24.25}_{1.39}$ pmol L^{-1}. These results indicate that the model values are in the range with observed concentrations of oceanic CHBr$_3$. While the mean concentration of the model is higher than the mean of the observations, all validated model data points fall within the full range of the observations. The model data cover a grid of ~100 km resolution, which leads to a smoothing of the values, whereas observational data is local daily mean point data.

The mean CHBr$_3$ atmospheric mixing ratio (Figure 4b) from the 697 daily mean observations is $1.45^{9.80}_{0.03}$ ppt. The global mean atmospheric mixing ratio of CHBr$_3$ from the model at locations with observations is $0.76^{2.70}_{0.22}$ ppt . This comparison shows that the observed atmospheric mixing ratios of CHBr$_3$ are in the same magnitude but generally higher than those from the model output. While our model experiment focuses on natural CHBr$_3$ production by phytoplankton, other sources as coastal macroalgae (Carpenter and Liss, 2000) and anthropogenic sources, such as power plant cooling (Maas et al., 2021) or desalination plants (Agus et al., 2009), may explain parts of the higher global annual median observational data of 41%. Jia et al. (2023) calculated an increase of global CHBr$_3$ emissions of 31.5% when including anthropogenic emissions, which partly can also explain the lower observed atmospheric mixing ratios in the model compared to the observations.

Figure 4 also shows a more detailed comparison between observations and model data in 5° meridional binned averages (shaded areas) for oceanic (Figure 4c) and atmospheric (Figure 4d) CHBr$_3$ on annual basis as well as in JJA and DJF. The modelled data compare well with observations of oceanic CHBr$_3$ (Figure 4c) on annual basis over the 5° latitudinal bins. In the HalOcAt database, there are no oceanic and atmospheric observations available north of 50°N and south of 30°S during boreal (DJF) and austral winter (JJA), respectively, which highlights the need of model data to entirely describe spatially and temporally resolved CHBr$_3$ (see also Fiehn et al., 2018). During DJF, the model overestimates the measured concentrations between 20°N and 5°S. During JJA, averaged model concentrations in the NH (10°N – 60°N) are slightly higher than the averaged observations. These discrepancies could indicate a missing process understanding, revealing lower oceanic production or additional loss processes.
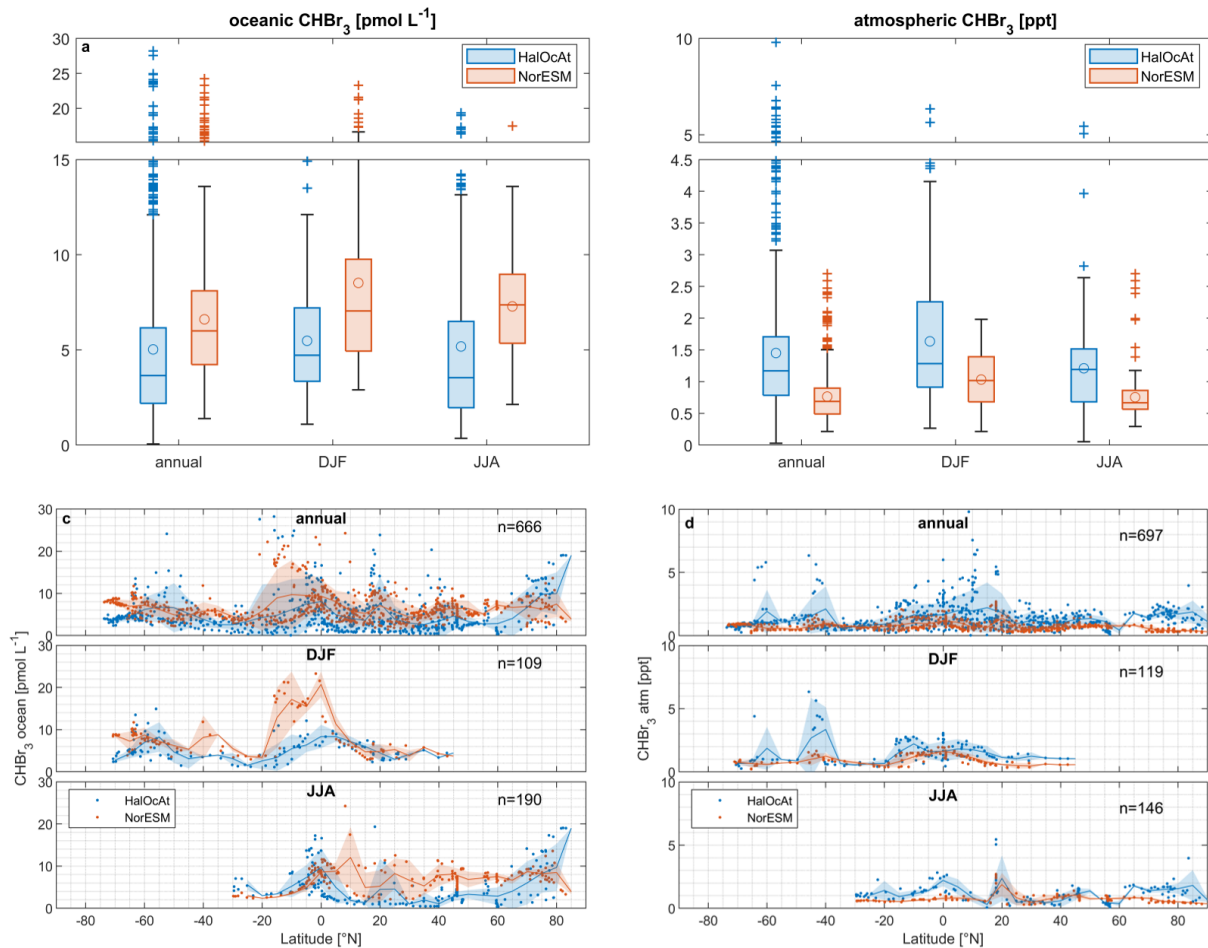
Figure 4: Boxplot comparison of NorESM2 model results with HalOcAt observations for oceanic (a) and atmospheric CHBr₃ (b), c: zonal mean oceanic CHBr₃ comparison annually and in DJF and JJA, d: zonal mean atmospheric CHBr₃ comparison annually and in DJF and JJA. Shaded areas are standard deviations from 5° zonal bin averages. Boxplots (left) have a break in the y axis to increase readability of the figure. The line inside the box represents the median value, the circle the mean value, the boxes show the first to third quartile, and the whiskers illustrate the highest and lowest values that are not outliers. The plus signs represent outliers.

296 With all data available, the 5° latitudinal averaged atmospheric CHBr₃ observations have a large spread in the tropics

297 resulting in a high standard deviation (Figure 4d). The model results in this region are uniform with a much lower standard

298 deviation. During boreal winter (DJF) atmospheric CHBr₃ observations and model results show a good agreement, with

299 an exception at 40-50°S. In this latitude range, observational atmospheric CHBr₃ mixing ratios (>3 ppt, Figure 4d) were

300 recorded between 24° and 60° W in the South Atlantic in 2007 (Gebhardt, 2008). Gebhardt (2008) reports enhanced

301 biological production in the Argentinian shelf-break zone (55°-60° W) with elevated chlorophyll-*a* concentration up to

302 4.5 µg L⁻¹. These values suggest also a high production of CHBr₃ and subsequent high emissions to the atmosphere. The

303 prevailing westerly winds, transported the CHBr₃ enriched air masses eastward to the remote South Atlantic region in

304 2007, while in the model lower biological production entails lower atmospheric mixing ratios compared to the

305 observations. During boreal summer (JJA) very good agreement between atmospheric observations and model results is

306 obtained between 10°N and 60°N. North of 60°N, the model underestimates the measured atmospheric mixing ratios in

307 the polar region. Local meteorological and biological conditions (e.g., high wind speed, distinct phytoplankton blooms)

308 are averaged by the model to a resolution of ~100 km. Averaging data over time or space leads to lower mean values (i.e.,

309 gas emissions, Bates and Merlivat, 2001) in the model. This explains lower modelled atmospheric mixing ratios compared

310 to the observations on a global scale together with anthropogenic CHBr₃ sources (Jia et al., 2023). Furthermore,

311 discrepancies between model results and observations also point to missing process understanding, which helps to

312 improve our understanding of the biogeochemical cycling of CHBr₃. For our CHBr₃ production rate, we used the highest

313 production rate, which we could retrieve from the published data (Roy, 2010; Kurihara et al., 2012). Therefore, we likely

314 do not underestimate the oceanic planktonic source in general, and either the production rates are too high or the sink

315 rates are too low in some regions, e.g., the equatorial Pacific. Furthermore, the resulting model bias does not follow a

316 spatial pattern (Fig. S4). We claim, that currently not enough observational or experimental information is available to

317 narrow down on the answer. As pointed out, the underestimation of atmospheric $CHBr_3$, despite the maximum of the

318 planktonic $CHBr_3$ source is likely due to averaging, a missing source for the atmosphere or even the parameterization of

319 marine $CHBr_3$ fluxes yielding too low emission values. Despite the named uncertainties, which deserve further studies,

320 the model reflects very well the data and therewith the current status of knowledge.

321 **3.3 Excess and deficit regions of oceanic bromoform**

322 In most of the world's surface oceans (e.g., North and South Pacific) $CHBr_3$ production and loss rates are balanced on an

323 annual average with a k_{bal} close to zero (top panel of Figure 5). The equator region experiences a strong excess rate

324 (positive k_{bal}) on annual average with values up to 300 pmol m^{-2} h^{-1} showing higher $CHBr_3$ production than loss of $CHBr_3$

325 in the upper ocean, caused by strong primary production (Fig. S3) in the equatorial upwelling. Surface currents transport

326 the $CHBr_3$ enriched surface water masses away from the equator, while experiencing loss of $CHBr_3$ to the atmosphere.

327 Therefore, adjacent marine areas north and south of the equator experience a deficit rate (negative k_{bal}) of $CHBr_3$ (blue

328 areas, Figure 5), as no production balances the loss. The seasonality of k_{bal} is pronounced in the extratropics (bottom

329 panels of Figure 5). In these regions, a $CHBr_3$ excess rate is observed mainly during summer and a $CHBr_3$ deficit rate

330 mainly during winter in the respective hemispheres. A high k_β (elevated biological production) and a low k_F (weak

331 emissions to the atmosphere) caused by lower winds during summer, lead to a higher $CHBr_3$ surface ocean concentration

332 in summer compared to winter time (Figure 3). During winter in both hemispheres, lower biological activity (low k_β) and

333 elevated wind speed (high k_F) decrease the $CHBr_3$ production and increase the emissions to the atmosphere, which leads

334 to a $CHBr_3$ deficit rate. These results reveal seasonal as well as spatial differences in parameters (driving factors), which

335 influence $CHBr_3$ concentrations in the world's ocean.

336 In the following subsection, we selected three different case study areas, indicated in Figure 5, in order to contrast the

337 driving factors of the variations of oceanic and atmospheric $CHBr_3$ on regional and temporal scales:

338 - North Atlantic, with an annual mean $CHBr_3$ deficit rate (k_{bal} = -33 pmol m^{-2} h^{-1})

339 - Tropical West Pacific, with an annual mean $CHBr_3$ excess rate (k_{bal} = +32 pmol m^{-2} h^{-1})

340 - Southern Ocean, with negative fluxes during the respective winter (k_{bal} = +15 pmol m^{-2} h^{-1})
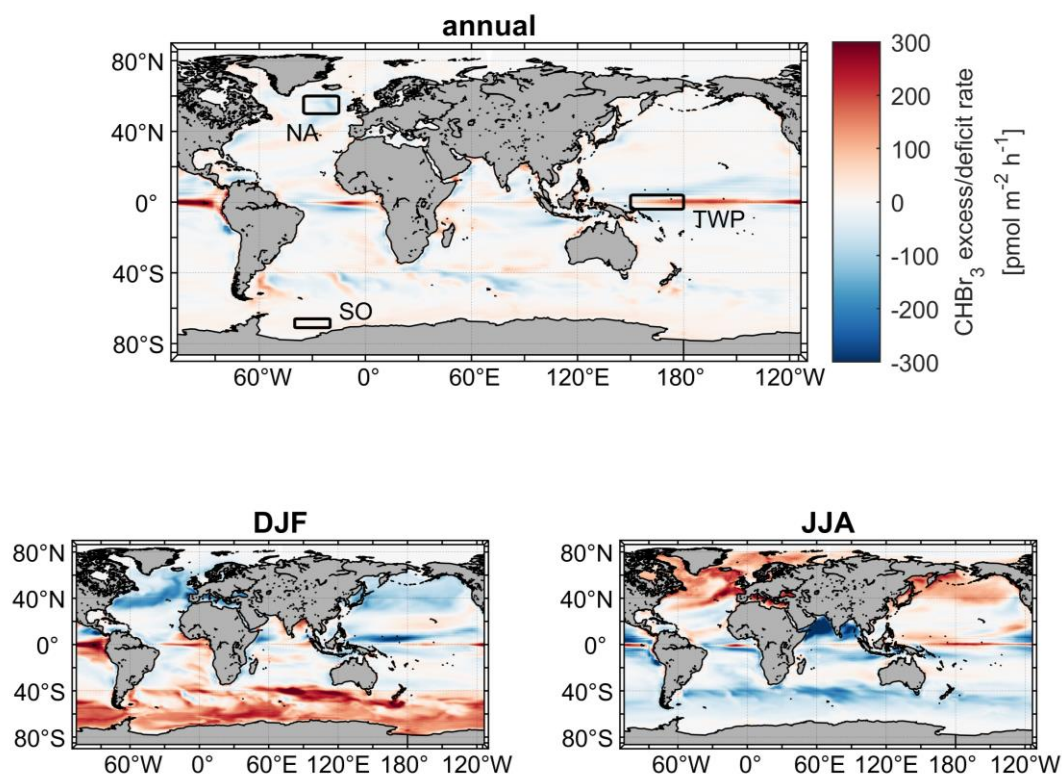
Figure 5: Mean CHBr₃ excess/deficit rates on annual (top) and seasonal (DJF: bottom left; JJA: bottom right) basis. Three rectangles in the top figure illustrate locations of case studies. NA: North Atlantic; TWP: Tropical West Pacific; SO: Southern Ocean.

3.4 Driving factors of bromoform on regional and temporal scales

This section investigates the seasonal changes of oceanic and atmospheric CHBr₃ and other parameters in three contrasting regions. Daily means of oceanic CHBr₃ concentrations, production, fluxes, balance (as defined in Eq. (15)), atmospheric mixing ratios as well as SST and wind speed, over an entire year reveal large differences between the North Atlantic, tropical West Pacific, and Southern Ocean (Figure 6). With MLR analysis, the main driving factors of oceanic and atmospheric CHBr₃ variability and its fluxes in each region and season are investigated.

347
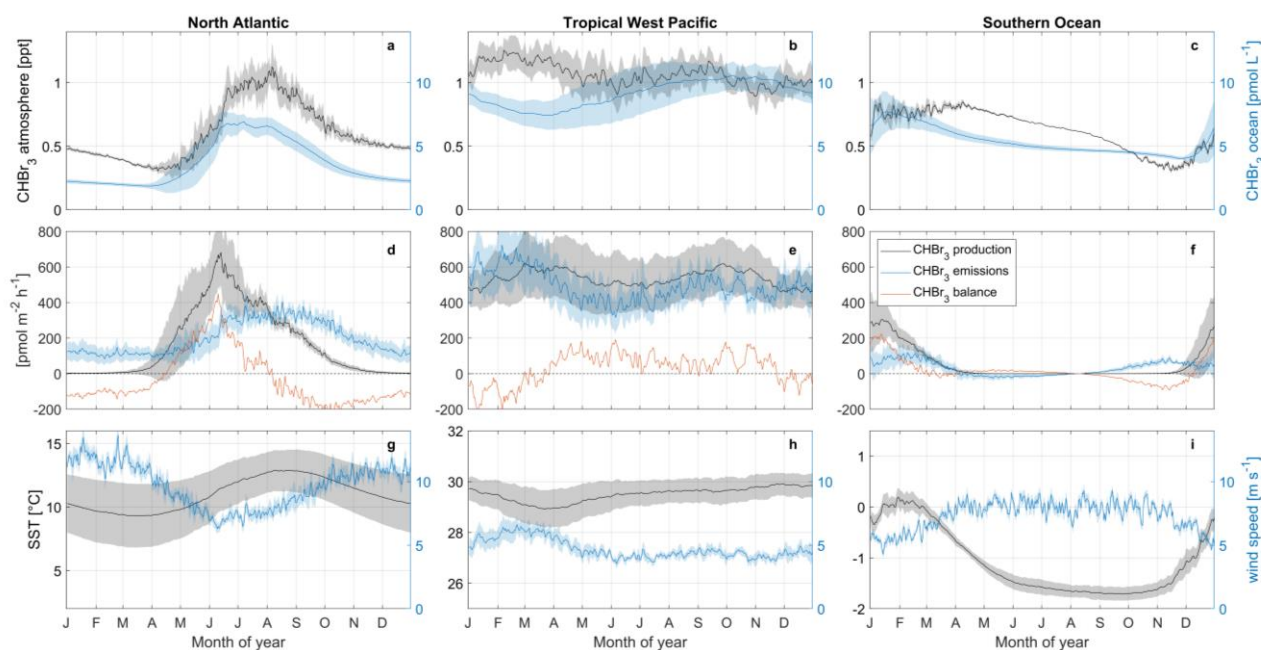
Figure 6: Seasonal changes of oceanic and atmospheric CHBr₃ (upper panel, a-c), CHBr₃ production, emissions and balance (middle panel, d-f), SST and wind speed (bottom panel, g-i), in the North Atlantic (left), tropical west Pacific (middle) and Southern Ocean (right). Shaded area is one standard deviation of the average value in the corresponding area. Note: y-limits for SST are not similar in between the three regions in order to increase readability of the figure.

348

North Atlantic

The North Atlantic region (50°N – 60°N, 15°W – 35°W) is characterized by a strong seasonal cycle of both oceanic CHBr₃ concentrations and atmospheric mixing ratios (Figure 6a). The magnitude of the cycle is strongest among the three investigated regions (compare with Figure 6b,c). Oceanic CHBr₃ concentrations are on average 3.64 pmol L^{-1} (min:1.87 pmol L^{-1} during end of March; max: 6.93 pmol L^{-1} during July). Atmospheric mixing ratios show a similar seasonal cycle, shifted by one month, with average values of 0.60 ppt, a minimum mixing ratio of 0.30 ppt during April and a maximum mixing ratio of 1.12 ppt during August. The CHBr₃ emissions (199±91 pmol m^{-2} h^{-1}) follow the pattern of both oceanic and atmospheric values (Figure 6d). The seasonal cycle of CHBr₃ production (171±191 pmol m^{-2} h^{-1}) is similar to the cycle of CHBr₃ concentration, while the sharp peak in May/June when the spring phytoplankton bloom evolves in the North Atlantic, is not reflected in the oceanic concentrations. The strong production leads to a CHBr₃ excess rate during summer (JJA: 103 pmol m^{-2} h^{-1}) and a CHBr₃ deficit rate in winter time (DJF: -114 pmol m^{-2} h^{-1}), respectively (Figure 6d).

The MLR analysis indicates, that on an annual basis, variations in atmospheric mixing ratios are mainly associated with CHBr3 ocean concentrations (Table 1,) and vice versa (Figure 7a,d). A higher surface water CHBr3 concentration increases the emissions to the atmosphere resulting in increasing atmospheric mixing ratios. According to the MLR analysis on a seasonal basis, oceanic CHBr3 concentrations are mainly driven by the oceanic production during MAM and SON (Table S1), which increases from March to June sharply to 680 pmol m-2 h-1 before gradually decreasing in SON (Figure 6d). Atmospheric mixing ratios are mainly driven by the oceanic concentration (Figure 7d, Table 1, R²=0.89, p-value<0.05). Only in winter (DJF), where hardly any production occurs, low SSTs, which increase the solubility of CHBr₃ drive the atmospheric mixing ratio variations (Table S1, R²=0.95, p-value<0.05). Thus, the emissions decrease, even during high wind speeds, which leads to lower atmospheric CHBr₃. The emissions are mainly driven by the oceanic concentrations (Figure 7g, Table 1, R²=0.81, p-value<0.05) over the course of a year, while during spring (MAM) wind speed, SST, and CHBr₃ production drive the emissions equally (Table S1). While CHBr₃ production and SSTs increase,

surface wind speed decreases and emissions are pretty constant at 130 ± 29 pmol m^{-2} h^{-1} (Figure 6d). During summer (JJA), low winds and a high oceanic CHBr$_3$ concentration equally increase the emissions (Table S1). In contrast to spring, higher SSTs (lower solubility) are only of minor importance during JJA, while in autumn and winter the decreasing SSTs are the main drivers again together with high atmospheric mixing ratios, which additionally dampen the emissions (Table S1).

Tropical West Pacific

Figure 5 shows that the equatorial regions of the Atlantic and Pacific Oceans are a source of oceanic CHBr$_3$, which is transported to other oceanic regions by ocean currents. CHBr$_3$ ocean concentrations in the tropical West Pacific (4°S – 4°N, 150°E – 180°E) show a reduced seasonal cycle in comparison to the above discussed North Atlantic region (Figure 6b), while the average of 9.11 pmol L^{-1} is significantly higher than in the North Atlantic. Also, CHBr$_3$ production (536±42 pmol m^{-2} h^{-1}), CHBr$_3$ fluxes (492±84 pmol m^{-2} h^{-1}) and atmospheric mixing ratios (1.07±0.08 ppt) show hardly any seasonality (Figure 6b, e). The same is true for SST (29.50±0.28 °C) and wind speed (4.71±0.76 m s^{-1}) (Figure 6h). The CHBr$_3$ balance is positive throughout the whole year except for DJF (Figure 6e). During this period high wind speed entails higher emission. Production rates are lower and induce a CHBr$_3$ deficit. However, this deficit does not compensate for the CHBr$_3$ excess during the rest of the year leading to an overall excess of 32 pmol m^{-2} h^{-1}.

MLR analysis shows that the wind speed is the main factor influencing the variations of oceanic CHBr$_3$ concentrations, CHBr$_3$ atmospheric mixing ratios, and CHBr$_3$ fluxes on an annual basis (Figure 7b,e,h, Table 1). During JJA and SON CHBr$_3$ production drives the CHBr$_3$ concentrations (Table S1) which increases from 477 pmol m^{-2} h^{-1} in July to 618 pmol m^{-2} h^{-1} by the end of September. This results in an increase of oceanic CHBr$_3$ concentrations as all other parameters stay constant during that period.

Southern Ocean

The selected Southern Ocean region (71°S – 66°S, 40°W – 20°W) experiences generally negative water temperatures (mean: -1.08°C) around the year (Figure 6i). The minimum of -1.71°C is reached in September and the maximum of +0.19°C in January/February. Wind speed is nearly constant throughout the year (7.33 m s^{-1}) decreasing only during austral summer (DJF, Figure 6h) to 5.76 m s^{-1}. Oceanic CHBr$_3$ concentrations are on average higher (5.38 pmol L^{-1}) than in the North Atlantic region. Maximum concentrations of 7.74 pmol L^{-1} are reached in January and lowest concentrations of 4.04 pmol L^{-1} end of December. Due to low SSTs as well as a short daylength, CHBr$_3$ production rates are almost zero from May to October and increase to 306 pmol m^{-2} h^{-1} in January (Figure 6f). Atmospheric mixing ratios are highest (0.85 ppt) from January to beginning of April and decline very slowly (Figure 6c) under the following low light levels until they reach their minimum of 0.31 ppt in November. Constant high atmospheric mixing ratios, very low SST, and decreasing oceanic CHBr$_3$ concentrations after the short summer bloom in DJF, influence the switch from emissions to negative fluxes between April and July (Figure 6f). CHBr$_3$ is in excess during times of production (DJF), almost balanced during the autumn and wintertime from April to September (Figure 6f), with a slight excess of 15 pmol m^{-2} h^{-1} annually.
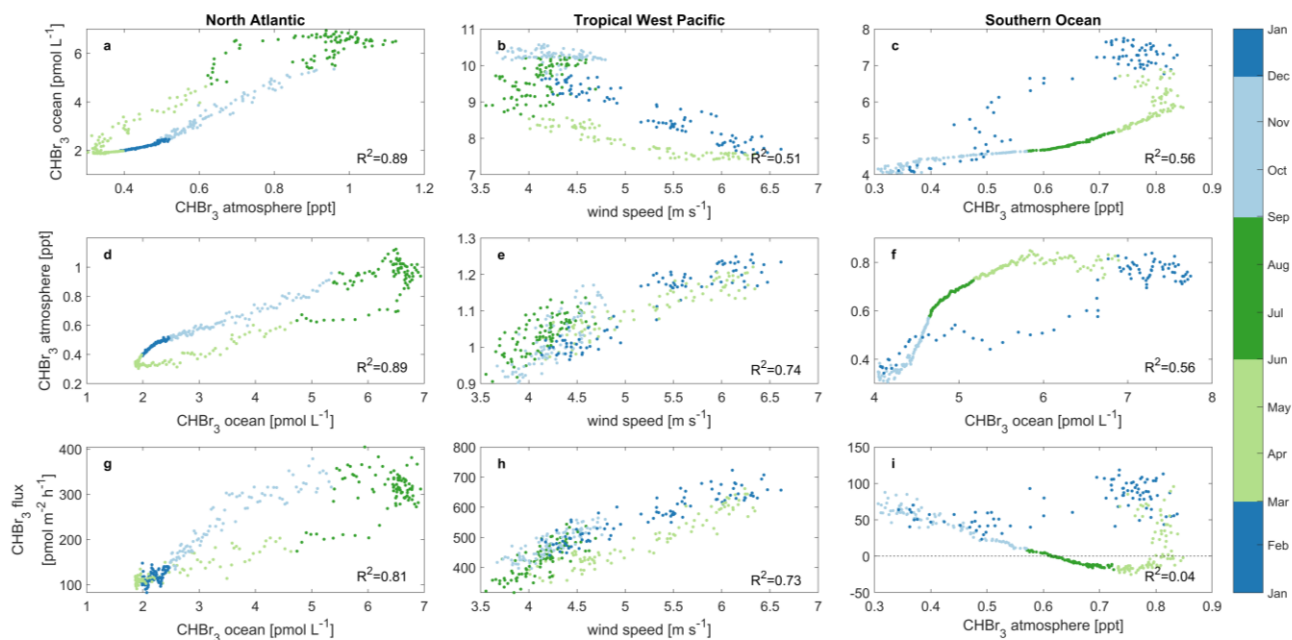
Figure 7: Main drivers of oceanic CHBr₃ concentrations (a, b, c), atmospheric mixing ratios (d, e, f) and CHBr₃ emissions (g, h, i) in the North Atlantic (a, d, g), tropical West Pacific (b, e, h) and Southern Ocean (c, f, i). Different colours denote different seasons of the year. Each data point represents a daily mean average over the specific case study area. Statistical analysis for each of the nine datasets indicates significant correlation (p-value<0.05) with coefficient of determination (R²) listed in bottom right of each sublot. Please be aware that subplots a and d as well as c and f contain the same information only with interchanged x and y axes, as both parameters, oceanic and atmospheric bromoform, are interdependent in the two regions.

405   Atmospheric mixing ratios are the main factor influencing the variations of oceanic concentrations (Figure 7c, Table 1,

406   R²=0.56, p-value<0.05), while during autumn (MAM, Table S1) CHBr₃ production is its driving factor. During this time

407   CHBr₃ production decreases and so does the ocean concentration (Figure 6c,f). The atmospheric mixing ratio is mainly

408   driven by high oceanic CHBr₃ concentrations in DJF: R²=0.88, p-value<0.05 and by SST during the cold JJA: R²=0.95,

409   p-value<0.05) (Table S1). Low light levels increase the lifetime of atmospheric CHBr₃ in JJA and the low SSTs increase

410   the solubility of oceanic CHBr₃, both leading to decreased emissions during winter (JJA). CHBr₃ emissions are mainly

411   driven by SST in summer (DJF) (Table S1, R²=0.60, p-value<0.05), as the solubility of CHBr₃ in the ocean decreases due

412   to the increasing SSTs. After this short summer period, temperatures decline in autumn (MAM) and increase the solubility

413   of oceanic CHBr₃, which results in decreased emissions (Figure 6f,i). During winter (JJA) and spring (SON), SSTs and

414   oceanic CHBr₃ concentrations stay low and therefore, increasing emissions are mainly driven by decreasing atmospheric

415   mixing ratios.

416

417   In summary, the three different regions clearly indicate that driving factors for atmospheric and oceanic bromoform as

418   well as for bromoform fluxes are dependent on local conditions. Planktonic production, which is the only source for

419   CHBr₃ in the model set-up impacts the variability of oceanic CHBr₃ concentrations only in regions with a distinct

420   seasonality (i.e., North Atlantic, Southern Ocean) in biological production. During times of lower productivity,

421   atmospheric mixing ratios influence the oceanic CHBr₃ concentration. In subpolar and polar regions (i.e., Southern

422   Ocean), oceanic CHBr₃ and its subsequent fluxes are driven by its solubility related to the low SST in late winter and

423   spring (i.e., sea-ice melt). Although wind speed is an important parameter for the air-sea gas flux, this study reveals that

424   wind speed is only the main driver for oceanic and atmospheric CHBr₃ variability in areas with low seasonality (i.e.,

425   Tropical West Pacific).

426   These results demonstrate the benefits of simulating CHBr₃ in a fully coupled ESM configuration to calculate driving

427   factors for different parameters on temporal and spatial basis. Studying the influence of one or more parameters on the

428   variability of other parameters in the model is not realistic when using prescribed oceanic concentrations or atmospheric

429 mixing ratios. Investigating the $CHBr_3$ cycling in different locations and different time scales helps to understand their

430 interconnection and to better integrate their results in today's as well as in a future climate.

431

432

433

434 **Table 1: Annual coefficients of predictors for each MLR in the different case studies. Bold coefficients are the highest value**
435 **within a MLR analysis of one parameter and region and act as indicator for the driving factors of the predicted parameter**
436 **(Eqs. S1-S3).**

	Predictor parameter	North Atlantic	Tropical West Pacific	Southern Ocean
$CHBr_3$ ocean concentration	Wind speed	-0.02	**-0.96**	-0.10
	SST	<0.01	<0.01	<0.01
	Atm. mixing ratio	**0.68**	0.19	**0.60**
	$CHBr_3$ production	0.39	0.13	0.53
	$CHBr_3$ fluxes	<0.01	<0.01	<0.01
$CHBr_3$ atmospheric mixing ratio	Wind speed	0.29	**0.94**	0.55
	SST	0.32	<0.01	<0.01
	Ocean concentration	**0.93**	0.12	**1.07**
	$CHBr_3$ production	<0.01	0.02	<0.01
	$CHBr_3$ fluxes	<0.01	<0.01	<0.01
$CHBr_3$ fluxes	Wind speed	0.20	**1.27**	0.21
	SST	0.67	0.50	0.53
	Ocean concentration	**0.83**	0.16	1.00
	$CHBr_3$ production	<0.01	0.10	<0.01
	Atm. mixing ratio	-0.32	-0.02	**-1.22**

437

438

3.5 Global bromoform emission inventories

440 A comparison of our modelled versus published global $CHBr_3$ emissions are presented in Figure 8. Global annual $CHBr_3$

441 emissions from top-down approaches are 449 Gg yr^{-1}, 528 Gg yr^{-1} and 592 Gg yr^{-1} based on calculations from Liang et

442 al. (2010), Ordóñez et al. (2012) and Warwick et al. (2006), respectively. These inventories are about two to eight times

443 higher than calculated annual emissions from bottom-up approaches, which are in the range of 76 Gg yr^{-1} (Stemmler et

444 al., 2015) to 238 Gg yr^{-1} (Lennartz et al., 2015). Our results (214 Gg yr^{-1}) are similar to emission estimates published by

445 Ziska et al. (2013) of 215 Gg yr^{-1} but significantly higher than the 76 Gg yr^{-1} estimate by Stemmler et al. (2015), which

446 is based on the oceanic $CHBr_3$ observations from HalOcAt.

447 As we apply a 2.38 higher $CHBr_3$ production rate in the ocean as Stemmler et al. (2015), we simulate a production rate

448 of 0.88 Gmol yr^{-1} compared to 0.37 Gmol yr^{-1} by Stemmler et al. (2015). Our emissions (214 Gg yr^{-1}) are 2.82 times

449 higher (Figure 8, global values) compared to the emission estimate (76 Gg yr^{-1}) from Stemmler et al. (2015). Our model

adaption is based on the higher bulk $CHBr_3$ production ratio (β_0) according to Kurihara et al. (2012) and Roy (2010) (see Section 2.1.1). This production rate is at the higher end of published values. Therefore, the resulting $CHBr_3$ production can be seen as an upper limit. Moreover, the ratio of bromoform emissions (ratio: 2.82) is higher compared to the ratio of bromoform production (ratio: 2.38) and indicates an excess of 18%. This is caused by the prescribed mean atmospheric values without any seasonality used in Stemmler et al. (2015) and gets more significant with higher latitudes where seasonality of bromoform emissions becomes more important (Fiehn et al., 2018). Especially during winter times annually mean prescribed atmospheric values are too high and artificially dampen the bromoform emissions. This results in a higher emission estimate using our fully coupled model approach.

Comparing bottom-up and top-down approaches, the annual $CHBr_3$ emissions from the tropics (20°S – 20°N, Figure 8) account for ~47% (105 Gg yr^{-1}) and ~66% (351 Gg yr^{-1}) of global emissions, respectively. The tropics only account for ~37% of global oceanic surface though, underlining this region as the most important source region of $CHBr_3$ of the earth. Emissions in the middle latitudes (20 to 50°N/S) of the NH and SH show a similar distinction between top-down and bottom-up approaches. However, the annual $CHBr_3$ emissions are only half that of the tropics. Natural open ocean emission estimates from our study are proportional to the surface area between NH and SH in the middle latitudes. This relationship is reversed for the top-down approach estimates. Top-down emission estimates are higher in the NH compared to the SH although the oceanic surface area is lower in the NH (17%) compared to the SH (26%). This indicates the strong influence of coastal emissions on observational atmospheric mixing ratios used in top-down approaches.

In the high latitudes (50-90°N/S), emissions of bottom-up approaches are in the same range (SH) and even higher (NH)

compared to top-down approaches (Figure 8). In the northern polar region (8% of global oceanic surface area), $CHBr_3$ emissions from our study account for 3% (6 Gg yr^{-1}) of global emissions and are significantly lower than the other two bottom-up approaches from Lennartz et al. (2015) (11%, 27 Gg yr^{-1}) and Ziska et al. (2013) (21%, 45 Gg yr^{-1}), which appears mainly due to the resolved seasonality within our study. According to the HalOcAt database, no measurements are recorded from November to February and from May to September north of 50°N in the NH and south of 50°S in the SH, respectively. Therefore, the prescribed atmospheric values in Ziska et al. (2013) and in

Figure 8: Comparison of global and latitudinally binned annual $CHBr_3$ emissions from different studies. Grey and blue bars denote top-down and bottom-up approaches, respectively.

Stemmler et al. (2015) are biased to the ice-free summer months, with higher atmospheric mixing ratios, thus artificially dampening the winter emissions. Due to the influence of the annually fixed prescribed atmospheric mixing ratios in Stemmler et al. (2015), negative fluxes are more pronounced between 50°N/S and 70°N/S up to -100 pmol m^{-2} h^{-1} at ~ 60°N/S. Our lesser negative fluxes in the coupled ESM approach appear more realistic as they are not based on summer biased prescribed values.

Our global $CHBr_3$ emission inventory indicates distinct differences to the top-down approaches reflecting only 40%-50% of global emissions calculated by Liang et al. (2010), Ordóñez et al. (2012) and Warwick et al. (2006). Atmospheric $CHBr_3$ values in the top-down approaches are higher than the calculated atmospheric mixing ratios from our fully coupled

492 model analysis. Those include elevated coastal sources (Scenario A and C, Liang et al., 2010), which may partly explain

493 the discrepancy.

494 An additional explanation for the overall higher atmospheric mixing ratios of $CHBr_3$ from observations could be that

495 observations from coastal areas (100 km within the coastline) were excluded from this study and are not represented in

496 the model, as they are difficult to quantify (i.e., tide-dependent $CHBr_3$ emissions of macroalgae) with a horizontal model

497 resolution of 1°. However, coastal emissions lead to higher atmospheric mixing ratios of $CHBr_3$ (Fuhlbrügge et al., 2013;

498 Fuhlbrügge et al., 2016; Hepach et al., 2016), which can be transported to remote open ocean regions, while these higher

499 observational values are not included in the model results (Figure 4).

500 Another explanation for the underestimation of the modelled atmospheric mixing ratios compared to observations is the

501 use of air-sea gas exchange parameterizations, whose uncertainty is estimated to be 25% (Wanninkhof, 2007) and may

502 be underestimated up to 75% (Yang et al., 2022) at low wind speeds.

503 **4   Conclusions and Outlook**

504 Our study is the first one to derive oceanic and atmospheric $CHBr_3$ concentrations, as well as fluxes, from a fully coupled

505 ESM simulation. The model prognostically simulates oceanic $CHBr_3$ production by phytoplankton and includes oceanic

506 $CHBr_3$ loss due to air-sea gas exchange, photolysis, hydrolysis and halogen substitution. Atmospheric loss of $CHBr_3$ is

507 attributed to photolysis and the reaction with OH. We validate the model results with more than 5,100 oceanic and 8,400

508 atmospheric observations from the HalOcAt database. The simulated global mean $CHBr_3$ emission rate (214 Gg yr^{-1}) is

509 in the range of previously published bottom-up approaches (76-238 Gg yr^{-1}), but significantly lower than top-down

510 approaches (449-592 Gg yr^{-1}). The model allows us to realistically resolve seasonal and spatial variations and to identify

511 different drivers of oceanic and atmospheric $CHBr_3$ variability on regional and seasonal scales. Our results indicate that

512 only during high productivity seasons a consequently high $CHBr_3$ production drives high oceanic $CHBr_3$ concentrations.

513 During low productivity seasons, relatively high atmospheric mixing ratios suppress gas exchange and consequently

514 influence variations in oceanic $CHBr_3$ concentrations. In tropical regions (e.g., tropical West Pacific), with a small

515 seasonal cycle, but high oceanic concentrations and atmospheric mixing ratios, wind speed is the main factor driving the

516 variability of oceanic and atmospheric $CHBr_3$ and its fluxes. The results clearly indicate the benefit of a fully coupled

517 ocean-atmosphere-biogeochemistry ESM. In earlier modelling studies, prescribed, fixed atmospheric or oceanic values

518 were applied, which bias the seasonal impact of different factors on oceanic and atmospheric $CHBr_3$ and subsequently

519 induce additional uncertainties to the magnitude of $CHBr_3$ emissions.

520 Our fully coupled ocean atmosphere approach resolves natural biogenic oceanic and atmospheric $CHBr_3$ concentrations,

521 and fluxes, at relatively high temporal and spatial model resolution. Validation with observational data shows good

522 agreement for large scale spatial patterns and we attribute the remaining model-data differences to missing coastal

523 sources, both natural and anthropogenic, which are not implemented in the model. Comparison with other published

524 $CHBr_3$ inventories indicates that approaches without seasonality do not resolve $CHBr_3$ fluxes, especially in high latitudes.

525 Our results demonstrate the potential for applying a fully coupled ESM to elucidate the primary drivers of the observed

526 $CHBr_3$ concentration and flux variability across spatial and temporal scales. Moreover, this model set-up allows us to

527 implement additional oceanic-derived VSLS, in order to further investigate their influence on atmospheric chemistry.

528 The dissociation of open ocean natural-derived $CHBr_3$ from coastal area-derived $CHBr_3$ in this study reveal that coastal-

529 derived $CHBr_3$ influences open ocean atmospheric mixing ratios. Therefore, implementing natural coastal and

530 anthropogenic sources along with high model resolution in these areas will help to further close the gap of published

531 $CHBr_3$ emission estimates between bottom-up and top-down approaches. Long-term future changes in $CHBr_3$ dynamics

532 under various scenarios should be investigated with a fully coupled ESM, in order to study the impact of climate change

533   on CHBr$_3$ dynamics, i.a., in the Arctic, associated with loss of sea-ice and its climate feedback through interaction with

534   ozone chemistry.

535

536   **Data availability.** Observational data can be made accessible by contacting the principal investigator of HalOcAt through

537   https://halocat.geomar.de. Model data will be archived and will be made available upon request.

538

539   **Author contributions.**

540   DB wrote the manuscript and led the discussion with contributions from all authors. DB analysed the model simulations

541   and prepared the graphics. JFT and DJLO implemented the CHBr$_3$ model code changes in NorESM2 in discussion with

542   BQ and all other authors. JFT carried out the model runs. KK led this project and initiated the research idea for this study.

543

544   **Competing interests.** The authors declare that they have no conflict of interest.

545

546   **Acknowledgements.** This work was financed by the Research Council of Norway through the KeyCLIM project

547   (295046) within the KLIMAFORSK/POLARFORSK program. Resources for the model simulations and data storage

548   were provided by Sigma2 - the National Infrastructure for High Performance Computing and Data Storage in Norway.

549

References

551   Agus, E., Voutchkov, N., and Sedlak, D. L.: Disinfection by-products and their potential impact on the quality of water
552   produced by desalination systems: A literature review, Desalination, 237, 214-237, 10.1016/j.desal.2007.11.059, 2009.

553   Assmann, K. M., Bentsen, M., Segschneider, J., and Heinze, C.: An isopycnic ocean carbon cycle model, Geoscientific
554   Model Development, 3, 143-167, DOI 10.5194/gmd-3-143-2010, 2010.

555   Bates, N. R. and Merlivat, L.: The influence of short-term wind variability on air-sea CO
556   exchange, Geophysical Research Letters, 28, 3281-3284, Doi 10.1029/2001gl012897, 2001.

557   Butler, J. H., King, D. B., Lobert, J. M., Montzka, S. A., Yvon-Lewis, S. A., Hall, B. D., Warwick, N. J., Mondeel, D. J.,
558   Aydin, M., and Elkins, J. W.: Oceanic distributions and emissions of short-lived halocarbons, Global Biogeochemical
559   Cycles, 21, Artn Gb1023
560   10.1029/2006gb002732, 2007.

561   Carpenter, L. J. and Liss, P. S.: On temperate sources of bromoform and other reactive organic bromine gases, Journal of
562   Geophysical Research-Atmospheres, 105, 20539-20547, Doi 10.1029/2000jd900242, 2000.

563   Danabasoglu, G., Lamarque, J. F., Bacmeister, J., Bailey, D. A., DuVivier, A. K., Edwards, J., Emmons, L. K., Fasullo,
564   J., Garcia, R., Gettelman, A., Hannay, C., Holland, M. M., Large, W. G., Lauritzen, P. H., Lawrence, D. M., Lenaerts, J.
565   T. M., Lindsay, K., Lipscomb, W. H., Mills, M. J., Neale, R., Oleson, K. W., Otto-Bliesner, B., Phillips, A. S., Sacks,
566   W., Tilmes, S., van Kampenhout, L., Vertenstein, M., Bertini, A., Dennis, J., Deser, C., Fischer, C., Fox-Kemper, B.,
567   Kay, J. E., Kinnison, D., Kushner, P. J., Larson, V. E., Long, M. C., Mickelson, S., Moore, J. K., Nienhouse, E., Polvani,
568   L., Rasch, P. J., and Strand, W. G.: The Community Earth System Model Version 2 (CESM2), Journal of Advances in
569   Modeling Earth Systems, 12, e2019MS001916, ARTN e2019MS001916
570   10.1029/2019MS001916, 2020.

571   Daniel, J. S., Solomon, S., Portmann, R. W., and Garcia, R. R.: Stratospheric ozone destruction: The importance of
572   bromine relative to chlorine, Journal of Geophysical Research-Atmospheres, 104, 23871-23880, Doi
573   10.1029/1999jd900381, 1999.

574   Dorf, M., Butler, J. H., Butz, A., Camy-Peyret, C., Chipperfield, M. P., Kritten, L., Montzka, S. A., Simmes, B., Weidner,
575   F., and Pfeilsticker, K.: Long-term observations of stratospheric bromine reveal slow down in growth, Geophysical
576   Research Letters, 33, Artn L24803
577   10.1029/2006gl027714, 2006.

Fiehn, A., Quack, B., Stemmler, I., Ziska, F., and Krüger, K.: Importance of seasonally resolved oceanic emissions for bromoform delivery from the tropical Indian Ocean and west Pacific to the stratosphere, Atmospheric Chemistry and Physics, 18, 11973-11990, 10.5194/acp-18-11973-2018, 2018.

Fuhlbrügge, S., Krüger, K., Quack, B., Atlas, E., Hepach, H., and Ziska, F.: Impact of the marine atmospheric boundary layer conditions on VSLS abundances in the eastern tropical and subtropical North Atlantic Ocean, Atmospheric Chemistry and Physics, 13, 6345-6357, 10.5194/acp-13-6345-2013, 2013.

Fuhlbrügge, S., Quack, B., Tegtmeier, S., Atlas, E., Hepach, H., Shi, Q., Raimund, S., and Krüger, K.: The contribution of oceanic halocarbons to marine and free tropospheric air over the tropical West Pacific, Atmospheric Chemistry and Physics, 16, 7569-7585, 10.5194/acp-16-7569-2016, 2016.

Gebhardt, S.: Biogenic emission of halocarbons, Mainz, Univ., Diss., 2008, 10.25358/openscience-2211, 2008.

Gettelman, A., Mills, M. J., Kinnison, D. E., Garcia, R. R., Smith, A. K., Marsh, D. R., Tilmes, S., Vitt, F., Bardeen, C. G., McInerny, J., Liu, H. L., Solomon, S. C., Polvani, L. M., Emmons, L. K., Lamarque, J. F., Richter, J. H., Glanville, A. S., Bacmeister, J. T., Phillips, A. S., Neale, R. B., Simpson, I. R., DuVivier, A. K., Hodzic, A., and Randel, W. J.: The Whole Atmosphere Community Climate Model Version 6 (WACCM6), Journal of Geophysical Research-Atmospheres, 124, 12380-12403, 10.1029/2019jd030943, 2019.

Gschwend, P. M., Macfarlane, J. K., and Newman, K. A.: Volatile halogenated organic compounds released to seawater from temperate marine macroalgae, Science, 227, 1033-1035, 10.1126/science.227.4690.1033, 1985.

Hense, I. and Quack, B.: Modelling the vertical distribution of bromoform in the upper water column of the tropical Atlantic Ocean, Biogeosciences, 6, 535-544, DOI 10.5194/bg-6-535-2009, 2009.

Hepach, H., Quack, B., Tegtmeier, S., Engel, A., Bracher, A., Fuhlbrügge, S., Galgani, L., Atlas, E. L., Lampel, J., Friess, U., and Krüger, K.: Biogenic halocarbons from the Peruvian upwelling region as tropospheric halogen source, Atmospheric Chemistry and Physics, 16, 12219-12237, 10.5194/acp-16-12219-2016, 2016.

Hossaini, R., Chipperfield, M. P., Montzka, S. A., Rap, A., Dhomse, S., and Feng, W.: Efficiency of short-lived halogens at influencing climate through depletion of stratospheric ozone, Nature Geoscience, 8, 186-190, 10.1038/Ngeo2363, 2015.

Jia, Y., Hahn, J., Quack, B., Jones, E., Brehon, M., and Tegtmeier, S.: Anthropogenic Bromoform at the Extratropical Tropopause, Geophysical Research Letters, 50, e2023GL102894, ARTN e2023GL102894 10.1029/2023GL102894, 2023.

Kurihara, M., Iseda, M., Ioriya, T., Horimoto, N., Kanda, J., Ishimaru, T., Yamaguchi, Y., and Hashimoto, S.: Brominated methane compounds and isoprene in surface seawater of Sagami Bay: Concentrations, fluxes, and relationships with phytoplankton assemblages, Marine Chemistry, 134, 71-79, 10.1016/j.marchem.2012.04.001, 2012.

Laube, J. C., Tegtmeier, S., Fernandez, R. P., Harrison, J., Hu, L., Krummel, P., Mahieu, E., Park, S., and Western, L.: Update on Ozone-Depleting Substances (ODSs) and Other Gases of Interest to the Montreal Protocol, 978-9914-733-97-6, 2023.

Law, K., Sturges, W., Blake, D., Blake, N., Burkholder, J., Butler, J., Cox, R., Haynes, P., Ko, M., and Kreher, K.: Halogenated very short-lived substances, Chapter 2 in: Scientific Assessment of Ozone Depletion: 2006, Global Ozone Research and Monitoring Project–Report No. 50, World Meteorological Organization, Geneva, Switzerland, 572, 2007.

Lennartz, S. T., Krysztofiak, G., Marandino, C. A., Sinnhuber, B. M., Tegtmeier, S., Ziska, F., Hossaini, R., Krüger, K., Montzka, S. A., Atlas, E., Oram, D. E., Keber, T., Bönisch, H., and Quack, B.: Modelling marine emissions and atmospheric distributions of halocarbons and dimethyl sulfide: the influence of prescribed water concentration vs. prescribed emissions, Atmospheric Chemistry and Physics, 15, 11753-11772, 10.5194/acp-15-11753-2015, 2015.

Liang, Q., Stolarski, R. S., Kawa, S. R., Nielsen, J. E., Douglass, A. R., Rodriguez, J. M., Blake, D. R., Atlas, E. L., and Ott, L. E.: Finding the missing stratospheric Br: a global modeling study of CHBr3 and CH2Br2, Atmospheric Chemistry and Physics, 10, 2269-2286, DOI 10.5194/acp-10-2269-2010, 2010.

Maas, J., Tegtmeier, S., Jia, Y., Quack, B., Durgadoo, J. V., and Biastoch, A.: Simulations of anthropogenic bromoform indicate high emissions at the coast of East Asia, Atmospheric Chemistry and Physics, 21, 4103-4121, 10.5194/acp-21-4103-2021, 2021.

625 Maier-Reimer, E.: Geochemical cycles in an ocean general circulation model. Preindustrial tracer distributions, Global
626 Biogeochemical Cycles, 7, 645-677, 10.1029/93gb01355, 2012.

627 Masson-Delmotte, V., Zhai, P., Pirani, A., Connors, S. L., Péan, C., Berger, S., Caud, N., Chen, Y., Goldfarb, L., Gomis,
628 M. I., Huang, M., Leitzell, K., Lonnoy, E., Matthews, J. B. R., Maycock, T. K., Waterfield, T., Yelekçi, O., Yu, R., Zhou,
629 B., and Ipcc: Annex I: Observational Products, in: Climate Change 2021 – The Physical Science Basis, Cambridge
630 University Press, Cambridge, United Kingdom and New York, NY, USA, 2061-2086, 10.1017/9781009157896.015,
631 2023.

632 Montzka, S. A., Reimann, S., Engel, A., Kruger, K., Sturges, W. T., Blake, D., Dorf, M., Fraser, P., Froidevaux, L., and
633 Jucks, K.: Ozone-depleting substances (ODSs) and related chemicals (chapter 1), 2011.

634 Moore, R. M., Geen, C. E., and Tait, V. K.: Determination of Henry's Law constants for a suite of naturally occurring
635 halogenated methanes in seawater, Chemosphere, 30, 1183-1191, 10.1016/0045-6535(95)00009-w, 1995.

636 Moore, R. M., Webb, M., Tokarczyk, R., and Wever, R.: Bromoperoxidase and iodoperoxidase enzymes and production
637 of halogenated methanes in marine diatom cultures, Journal of Geophysical Research-Oceans, 101, 20899-20908, Doi
638 10.1029/96jc01248, 1996.

639 Navarro, M. A., Atlas, E. L., Saiz-Lopez, A., Rodriguez-Lloveras, X., Kinnison, D. E., Lamarque, J. F., Tilmes, S., Filus,
640 M., Harris, N. R., Meneguz, E., Ashfold, M. J., Manning, A. J., Cuevas, C. A., Schauffler, S. M., and Donets, V.: Airborne
641 measurements of organic bromine compounds in the Pacific tropical tropopause layer, Proc Natl Acad Sci U S A, 112,
642 13789-13793, 10.1073/pnas.1511463112, 2015.

643 Nightingale, P. D., Malin, G., Law, C. S., Watson, A. J., Liss, P. S., Liddicoat, M. I., Boutin, J., and Upstill-Goddard, R.
644 C.: In situ evaluation of air-sea gas exchange parameterizations using novel conservative and volatile tracers, Global
645 Biogeochemical Cycles, 14, 373-387, Doi 10.1029/1999gb900091, 2000.

646 Ordóñez, C., Lamarque, J. F., Tilmes, S., Kinnison, D. E., Atlas, E. L., Blake, D. R., Sousa Santos, G., Brasseur, G., and
647 Saiz-Lopez, A.: Bromine and iodine chemistry in a global chemistry-climate model: description and evaluation of very
648 short-lived oceanic sources, Atmospheric Chemistry and Physics, 12, 1423-1447, 10.5194/acp-12-1423-2012, 2012.

649 Papanastasiou, D. K., McKeen, S. A., and Burkholder, J. B.: The very short-lived ozone depleting substance CHBr
650 (bromoform): revised UV absorption spectrum, atmospheric lifetime and ozone depletion potential, Atmospheric
651 Chemistry and Physics, 14, 3017-3025, 10.5194/acp-14-3017-2014, 2014.

652 Quack, B. and Wallace, D. W. R.: Air-sea flux of bromoform: Controls, rates, and implications, Global Biogeochemical
653 Cycles, 17, 10.1029/2002gb001890, 2003.

654 Quack, B., Atlas, E., Petrick, G., Stroud, V., Schauffler, S., and Wallace, D. W. R.: Oceanic bromoform sources for the
655 tropical atmosphere, Geophysical Research Letters, 31, Artn L23s05
656 10.1029/2004gl020597, 2004.

657 Roy, R.: Short-term variability in halocarbons in relation to phytoplankton pigments in coastal waters of the central
658 eastern Arabian Sea, Estuarine Coastal and Shelf Science, 88, 311-321, 10.1016/j.ecss.2010.04.011, 2010.

659 Saiz-Lopez, A., Fernandez, R. P., Li, Q., Cuevas, C. A., Fu, X., Kinnison, D. E., Tilmes, S., Mahajan, A. S., Gomez
660 Martin, J. C., Iglesias-Suarez, F., Hossaini, R., Plane, J. M. C., Myhre, G., and Lamarque, J. F.: Natural short-lived
661 halogens exert an indirect cooling effect on climate, Nature, 618, 967-973, 10.1038/s41586-023-06119-z, 2023.

662 Sala, S., Bönisch, H., Keber, T., Oram, D. E., Mills, G., and Engel, A.: Deriving an atmospheric budget of total organic
663 bromine using airborne in situ measurements from the western Pacific area during SHIVA, Atmospheric Chemistry and
664 Physics, 14, 6903-6923, 10.5194/acp-14-6903-2014, 2014.

665 Salawitch, R. J.: Atmospheric chemistry: biogenic bromine, Nature, 439, 275-277, 10.1038/439275a, 2006.

666 Sinnhuber, B. M., Sheode, N., Sinnhuber, M., Chipperfield, M. P., and Feng, W.: The contribution of anthropogenic
667 bromine emissions to past stratospheric ozone trends: a modelling study, Atmospheric Chemistry and Physics, 9, 2863-
668 2871, DOI 10.5194/acp-9-2863-2009, 2009.

669 Stemmler, I., Hense, I., and Quack, B.: Marine sources of bromoform in the global open ocean - global patterns and
670 emissions, Biogeosciences, 12, 1967-1981, 10.5194/bg-12-1967-2015, 2015.

671 Tegtmeier, S., Atlas, E., Quack, B., Ziska, F., and Krüger, K.: Variability and past long-term changes of brominated very
672 short-lived substances at the tropical tropopause, Atmospheric Chemistry and Physics, 20, 7103-7123, 10.5194/acp-20-
673 7103-2020, 2020.

674 Tjiputra, J. F., Assmann, K., Bentsen, M., Bethke, I., Otterå, O. H., Sturm, C., and Heinze, C.: Bergen Earth system model
675 (BCM-C): model description and regional climate-carbon cycle feedbacks assessment, Geoscientific Model
676 Development, 3, 123-141, DOI 10.5194/gmd-3-123-2010, 2010.

677 Tjiputra, J. F., Schwinger, J., Bentsen, M., Morée, A. L., Gao, S., Bethke, I., Heinze, C., Goris, N., Gupta, A., He, Y. C.,
678 Olivié, D., Seland, O., and Schulz, M.: Ocean biogeochemistry in the Norwegian Earth System Model version 2
679 (NorESM2), Geoscientific Model Development, 13, 2393-2431, 10.5194/gmd-13-2393-2020, 2020.

680 Tokarczyk, R. and Moore, R. M.: Production of Volatile Organohalogens by Phytoplankton Cultures, Geophysical
681 Research Letters, 21, 285-288, Doi 10.1029/94gl00009, 1994.

682 Villamayor, J., Iglesias-Suarez, F., Cuevas, C. A., Fernandez, R. P., Li, Q. Y., Abalos, M., Hossaini, R., Chipperfield, M.
683 P., Kinnison, D. E., Tilmes, S., Lamarque, J. F., and Saiz-Lopez, A.: Very short-lived halogens amplify ozone depletion
684 trends in the tropical lower stratosphere, Nature Climate Change, 13, 554-+, 10.1038/s41558-023-01671-y, 2023.

685 Wang, S. Y., Kinnison, D., Montzka, S. A., Apel, E. C., Hornbrook, R. S., Hills, A. J., Blake, D. R., Barletta, B., Meinardi,
686 S., Sweeney, C., Moore, F., Long, M., Saiz-Lopez, A., Fernandez, R. P., Tilmes, S., Emmons, L. K., and Lamarque, J.
687 F.: Ocean Biogeochemistry Control on the Marine Emissions of Brominated Very Short-Lived Ozone-Depleting
688 Substances: A Machine-Learning Approach, Journal of Geophysical Research-Atmospheres, 124, 12319-12339,
689 10.1029/2019jd031288, 2019.

690 Wanninkhof, R.: The Impact of Different Gas Exchange Formulations and Wind Speed Products on Global Air-Sea CO2
691 Fluxes, in: Transport at the Air-Sea Interface, edited by: Garbe, C. S., Handler, R. A., and Jähne, B., Environmental
692 Science and Engineering, Springer Berlin Heidelberg, Berlin, Heidelberg, 1-23, 10.1007/978-3-540-36906-6_1, 2007.

693 Warwick, N. J., Pyle, J. A., Carver, G. D., Yang, X., Savage, N. H., O'Connor, F. M., and Cox, R. A.: Global modeling
694 of biogenic bromocarbons, Journal of Geophysical Research-Atmospheres, 111, Artn D24305
695 10.1029/2006jd007264, 2006.

696 Washington, J. W.: Hydrolysis Rates of Dissolved Volatile Organic-Compounds - Principles, Temperature Effects and
697 Literature-Review, Ground Water, 33, 415-424, DOI 10.1111/j.1745-6584.1995.tb00298.x, 1995.

698 Yang, M. X., Bell, T. G., Bidlot, J. R., Blomquist, B. W., Butterworth, B. J., Dong, Y. X., Fairall, C. W., Landwehr, S.,
699 Marandino, C. A., Miller, S. D., Saltzman, E. S., and Zavarsky, A.: Global Synthesis of Air-Sea CO
700 Transfer Velocity Estimates From Ship-Based Eddy Covariance Measurements, Front. Mar. Sci., 9, ARTN 826421
701 10.3389/fmars.2022.826421, 2022.

702 Ziska, F., Quack, B., Abrahamsson, K., Archer, S. D., Atlas, E., Bell, T., Butler, J. H., Carpenter, L. J., Jones, C. E.,
703 Harris, N. R. P., Hepach, H., Heumann, K. G., Hughes, C., Kuss, J., Krüger, K., Liss, P., Moore, R. M., Orlikowska, A.,
704 Raimund, S., Reeves, C. E., Reifenhäuser, W., Robinson, A. D., Schall, C., Tanhua, T., Tegtmeier, S., Turner, S., Wang,
705 L., Wallace, D., Williams, J., Yamamoto, H., Yvon-Lewis, S., and Yokouchi, Y.: Global sea-to-air flux climatology for
706 bromoform, dibromomethane and methyl iodide, Atmospheric Chemistry and Physics, 13, 8915-8934, 10.5194/acp-13-
707 8915-2013, 2013.
708